Food Structure 40 (2024) 100365

Contents lists available at ScienceDirect

Food Structure

journal homepage: www.elsevier.com/locate/foostr

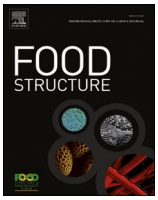

Adapting cryogenic correlative light and electron microscopy (cryo-CLEM) for food oxidation studies

Suyeon Yang [a,1], Machi Takeuchi [b,c,1], Rick R.M. Joosten [b,d], John P.M. van Duynhoven [a,e,*], Heiner Friedrich [b,c,d,**], Johannes Hohlbein [a,f,*]

[a] Laboratory of Biophysics, Wageningen University and Research, Stippeneng 4, 6708 WE Wageningen, the Netherlands
[b] Laboratory of Physical Chemistry, Department of Chemical Engineering and Chemistry, Eindhoven University of Technology, P.O. Box 513, 5600 MB Eindhoven, the Netherlands
[c] Institute for Complex Molecular Systems, Eindhoven University of Technology, P.O. Box 513, 5600 MB Eindhoven, the Netherlands
[d] Center for Multiscale Electron Microscopy, Department of Chemical Engineering and Chemistry, Eindhoven University of Technology, Het Kranenveld 14, 5600 MB Eindhoven, the Netherlands
[e] Unilever Global Foods Innovation Centre, Bronland 14, 6708 WH Wageningen, the Netherlands
[f] Microspectroscopy Research Facility, Wageningen University and Research, Stippeneng 4, 6708 WE Wageningen, the Netherlands

ARTICLE INFO

Keywords:
Correlative imaging
Cryogenic temperature
Heterogeneity
Interface
Lipid oxidation
Protein aggregates

ABSTRACT

Lipid oxidation is a major cause of product deterioration in protein stabilised oil-in-water food emulsions. The impact of protein emulsifiers on lipid oxidation and the stability depends on the specific type of protein emulsifiers used and the redox conditions in the emulsion. However, the exact impact of these protein emulsifiers at the oil-water interface on lipid oxidation and the mechanism of lipid-protein co-oxidation are currently unknown. Here, we developed a cryo-correlative light and electron microscopy (cryo-CLEM) platform for co-localising the oxidation of lipids and proteins. For this first implementation of cryo-CLEM for food oxidation studies we optimised specifically the part of cryo-fluorescence microscopy (cryo-FM) by adding parts that prevent fogging on the sample and enable homogeneous laser illumination. We showed that lipid oxidation in food emulsions can be observed at cryogenic temperature using fluorescence imaging of the fluorophore BODIPY 665/676 that we employed earlier as a lipid oxidation sensor at room temperature. Using cryo-transmission electron microscopy (cryo-TEM), we observed that more protein aggregates are found at the droplet interfaces in oxidized emulsions compared to fresh emulsions. Our cryo-CLEM platform paves the way for future cryo-correlative oxidation studies of food emulsions.

1. Introduction

Many food products such as mayonnaise, salad dressings, and cream cheese are oil-in-water (O/W) emulsions that are commonly stabilized with emulsifiers consisting of proteins and amphiphilic lipid surfactants (McClements, 2015). In O/W food emulsions, lipid oxidation is widely considered a key factor for food deterioration (McClements & Decker, 2000). The role of the emulsifiers at the interface is, however, poorly understood, even though lipid oxidation is thought to be initiated there (Berton-Carabin et al., 2014). Specifically, it is currently unclear, what the exact role of proteins at the interface on lipid oxidation is (Berton-Carabin et al., 2014, 2018a). Whereas some earlier work showed that protein-stabilized interfaces are less efficient at protecting emulsified lipids against oxidation than those stabilized with low-molecular weight surfactants (Berton, Ropers, et al., 2011), other studies indicated that proteins at the interface act as antioxidants (Yang & Xiong, 2015; Zhu et al., 2018). Therefore, understanding lipid-protein co-oxidation at the interface is essential for addressing food deterioration. However, not many studies have addressed this aspect so far due to a lack of experimental methods that allow the co-localisation of lipid oxidation and proteins at the O/W interface.

To address this methodology gap, we adapted a cryogenic correlative

* Corresponding authors at: Laboratory of Biophysics, Wageningen University and Research, Stippeneng 4, 6708 WE Wageningen, the Netherlands.
** Corresponding author at: Laboratory of Physical Chemistry, Department of Chemical Engineering and Chemistry, Eindhoven University of Technology, P.O. Box 513, 5600 MB Eindhoven, the Netherlands.
E-mail addresses: john.vanduynhoven@wur.nl (J.P.M. van Duynhoven), H.Friedrich@tue.nl (H. Friedrich), johannes.hohlbein@wur.nl (J. Hohlbein).
[1] These authors contributed equally.

https://doi.org/10.1016/j.foostr.2024.100365
Received 28 November 2023; Received in revised form 25 January 2024; Accepted 30 January 2024
Available online 5 February 2024

light and electron microscopy (cryo-CLEM) platform for studying oxidation in food emulsions. CLEM is an emerging technique that combines information from fluorescence microscopy and electron microscopy performed at similar regions within a sample (Brown & Verkade, 2010; Giepmans, 2008; Mironov & Beznoussenko, 2009; Muller-Reichert & Verkade, 2014; van Elsland, Bos, Overkleeft, Koster, & van Kasteren, 2015). CLEM has been developed and applied mainly in the life science allowing, for example, the correlation of nanoscale structural information with the localisation of specific, fluorophore-labelled biomolecules (de Boer et al., 2015; Wolff et al., 2016). Correlative imaging approaches are also relevant in other scientific fields such as polymer science (Wang et al., 2021). For performing transmission electron microscopy (TEM) at native conditions, CLEM typically requires laborious sample preparation steps such as chemical fixation, staining, resin embedding, and cutting, all of which may lead to potential artifacts (Ayache et al., 2010; Murk et al., 2003; Schnell et al., 2012). The use of chemical fixatives can be circumvented by utilizing rapid cooling of samples, such as with plunge vitrification (Schultz, 1988) or high-pressure freezing (Dahl & Staehelin, 1989) and measuring the samples at cryogenic temperatures. In fact, it has been reported that cryo-fixated samples expose better preserved structures as compared to chemically fixated samples (Dahl & Staehelin, 1989; Murk et al., 2003; Steinbrecht & Zierold, 2012).

Sample vitrification and microscopy observation at low temperatures are especially helpful for food emulsions as cryogenic temperatures prevent the diffusion of components and further oxidation during measurements. Despite its apparent potential, Cryo-CLEM has not yet been employed for studying food systems. More specifically, the length scales covered by CLEM (nm to μm scale) have the potential to provide insights into the relationship between the (co-) oxidation of lipids and proteins at droplet interfaces and the local nanoscale arrangement of proteins. In previous work, we showed aggregation of proteins in the continuous phase separated from mayonnaise using localisation of fluorescently labelled spin-traps and autofluorescence by room temperature (RT)-confocal microscopy and cryo-TEM (Yang, Takeuchi, et al., 2023). We could observe aggregation of proteins in the aqueous phase upon oxidation, however, without employing fluorescence microscopy and cryo-TEM in a correlative manner.

Here, we build on our previous work and image the lipid oxidation of oil droplets in fluorescence microscopy at cryogenic temperatures. We first introduce a home-built cryo-upright fluorescence microscope (cryo-FM) for correlative imaging and test the setup with fluorescent beads. We then demonstrate fluorescence detection of an oxidation-sensitive dye, BODIPY 665/676, in egg yolk stabilized model emulsions at cryogenic temperature (77 K). In addition, we observe protein granules at the oil droplet interfaces of fresh and oxidized emulsions using cryo-TEM. Finally, we demonstrate correlative imaging of the model emulsion using both cryo-FM and cryo-TEM on the same sample region. Our work demonstrates the feasibility of using cryo-CLEM to unravel the role of colloidal interfacial structure in mediating lipid oxidation of food emulsions by correlating images from cryo-FM and cryo-TEM.

2. Materials and methods

2.1. Materials

Soybean oil and egg yolk containing 8 % (w/w) NaCl were purchased from a local store. The lipophilic oxidation-sensitive dye BODIPY 665/676 and Cy3 dye were purchased from Thermo Fischer (Waltham, MA, USA). Alumina power (Alumina N—Super I) was obtained from MP EcoChrom (Eschwege, Germany). Fluorescent beads with a diameter of 200 and 780 nm were purchased from ThermoFisher Scientific (Eugene, Oregon, USA) and Bangs Laboratories, Inc (Indiana, USA), respectively. Sodium acetate (MW: 82.03 g/mol), Acetic Acid (MW: 60.05 g/mol), and 2,2′-Azobis (2-amidinopropane) dihydrochloride (AAPH) were purchased from Sigma-Aldrich (Zwijndrecht, the Netherlands). Ultrapure water (18.2 MΩ) was used and prepared using a Milli-Q system (Millipore Corporation, Billerica, MA, USA). Dimethyl sulfoxide (DMSO) was purchased from Thermo Fisher (Waltham, MA, USA).

2.2. Preparation of emulsions

0.05 M of acetate buffer (pH 3.8) was prepared with sodium acetate (0.6 g) and acetic acid (2.6 g) in 1 L of ultrapure water. For the preparation of the continuous phase, egg yolk was mixed in the buffer with a concentration of 1 wt %. Stripped soybean oil was prepared using alumina powder to remove impurities and lipid-soluble antioxidants (Berton, Genot, et al., 2011). Briefly, the oil was mixed with the powder at a volume ratio of 2:1 in Falcon tubes and shaken for 24 hrs. The suspension was then centrifuged at 2000 $\times g$ for 20 min. The oil was collected, and the same centrifugation procedure was repeated to ensure the complete removal of the alumina powder. For providing a marker of lipid oxidation, 50 μM of BODIPY 665/676 was pre-mixed in the stripped soybean oil before making emulsions. A coarse emulsion was first prepared by adding 10 wt % of stripped soybean oil to the continuous phase, and high-speed stirring was applied at 11,000 rpm for 1 min with a rotor-stator homogenizer (Ultra-turrax IKA T18 basic, Germany). Next, a fine emulsion was prepared by passing the coarse emulsion through either, (i), a lab-scale colloid mill with a gap width of 0.32 mm (IKA Magic Lab, Staufen, Germany), operating for 1 min at 26,000 rpm or, (ii), a microfluidizer (Microfluidics, Massachusetts, USA), equipped with a Y-shaped interaction chamber (F12Y; minimum internal dimension: 75 μm), operating at 600 bars during three passes. During the operation, the colloid mill was cooled with water at 4 °C, and for the microfluidizer, the sample chamber was placed in an ice bath. Oxidization was induced by incubating 1 mL of emulsions at 40 °C with 5 mM of the radical initiator (AAPH) in the dark over two days.

2.3. Cryo sample preparation

Cryo-samples were prepared as follows: (i) Prior to the application of the sample, TEM grids were first surface plasma treated for 40 s using a Cressington 208 carbon coater to make the surface of the carbon TEM support film hydrophilic. Two different TEM grids were used in the experiments; either a 200 mesh Cu TEM grid with a R2/2 Quantifoil® carbon support film (Quantifoil MicroTools GmbH) or a 200 mesh Au TEM finder grid with a R2/2 Quantifoil® carbon support film (LFH2100AR2, AURION). (ii) Samples of either the fluorescent beads or emulsions were first diluted tenfold with buffer to control the density of oil droplets and provide more suitable conditions for cryo-TEM imaging. Then, 3 μl of the diluted samples were applied on TEM grids in an automated vitrification robot (Thermo Fisher Scientific Vitrobot™ Mark IV). Samples were blotted with a blotting time of 3 s and blot force of − 4 and subsequently plunged into liquid ethane. Prior to further measurements, all vitrified samples were stored in a grid box at 77 K in a liquid nitrogen tank.

2.4. Optical setup of cryo-FM and cryo-TEM

For cryo-FM measurements, a cryo-stage was purchased from LINKAM (CMS196M, UK), and a laser was obtained from Integrated Optics (MatchBox, 405, 520, and 638 nm, Lithuania). A square-core multimode fibre (0.39 NA, 150 × 150 μm square core), an iris (SM1D12D), a lens for the collimation (f = 50 mm, AC254–050-A), mirrors (BBE1-E02), a second lens (f = 250 mm, AC254–250-A), a dichroic mirror holder (DMF1/M), motorized Translation Stage for z-focusing (KMTS25E/M), and a tube lens (f = 200 mm, ITL 200) were all purchased from Thorlabs (Germany). A dichroic mirror (ZT532/640rpc-UF2) and a bandpass filter (ZET532/640 m-TRF) were obtained from Chroma (USA). The objective (100x, NA 0.90, WD 2.0 mm, MUC11900) was purchased from Nikon (Japan), and the camera (UI-3060CP-M-GL R2) from IDS (Germany). Vibration motors (MF-6318927,

MAKERFACTORY) were obtained from Conrad Electronic (Germany).

Cryo-TEM imaging was conducted on the TU/e CryoTitan (Thermo Fisher Scientific), which was operated at 300 kV and is equipped with a Field-Emission Gun, a post-column Gatan Energy Filter (GIF, model 2002) and a post-GIF 2k × 2k Gatan CCD camera (model 794). Cryo-TEM images were recorded at a nominal defocus of − 20 μm and − 5 μm for nominal magnifications of 6500× and 24,000×, respectively.

3. Results and discussion

3.1. Design of the correlative cryo-FM and cryo-TEM platform

For correlative imaging, here combining cryogenic fluorescence microscopy (cryo-FM) and cryogenic transmission electron microscopy (cryo-TEM), we developed the following workflow (Fig. 1). First, we prepared the vitrified samples described in Section 2.3 (Fig. 1a). Then, we transferred the vitrified specimen to the LINKAM cryo-stage and obtained cryo-FM images (Fig. 1b). The sample loading step is conducted in the LINKAM cryo-stage, from a grid box to the loading station, then to the sample stage. The EM grid is inserted into the sample magnet clamp in the loading station, which is then loaded on the sample stage. The liquid nitrogen (LN_2) reservoir is connected to the stage, keeping the temperature of the sample stage at 77 K. A list of the optical components for cryo-FM is given in Section 2.4, and the optical setup will be elucidated in the next section. After the measurements in cryo-FM, we transferred the sample to cryo-TEM. Cryo-TEM is conducted on the same regions identified by cryo-FM. We used the holey carbon film to increase the contrast, and a brief explanation of cryo-TEM is provided in Fig. 1c. Accelerated electron beams generally travel through three sets of electromagnetic lenses (condenser, objective, and projection lenses) before the magnified image of a specimen is obtained (Kuo, 2007; van Huis & Friedrich, 2014).

3.2. Implementation of a cryogenic fluorescence microscopy (cryo-FM) platform

Fluorescence microscopy is often performed on inverted microscopes as this arrangement improves the stability of the optical setup and imposes less limitations on sample weight or height. Here, due to the need for having liquid nitrogen close to the sample to reach cryogenic temperatures, an upright microscope configuration was built above a LINKAM cryo-stage (Fig. 2a). The laser is coupled in a square-core multimode fibre with vibration motors to obtain a homogeneous intensity beam distribution. After the fibre, an iris (aperture) was placed to adjust the diameter of the beam. The laser beam is collimated with a lens and reflected by mirrors to an additional lens, which is inserted for beam

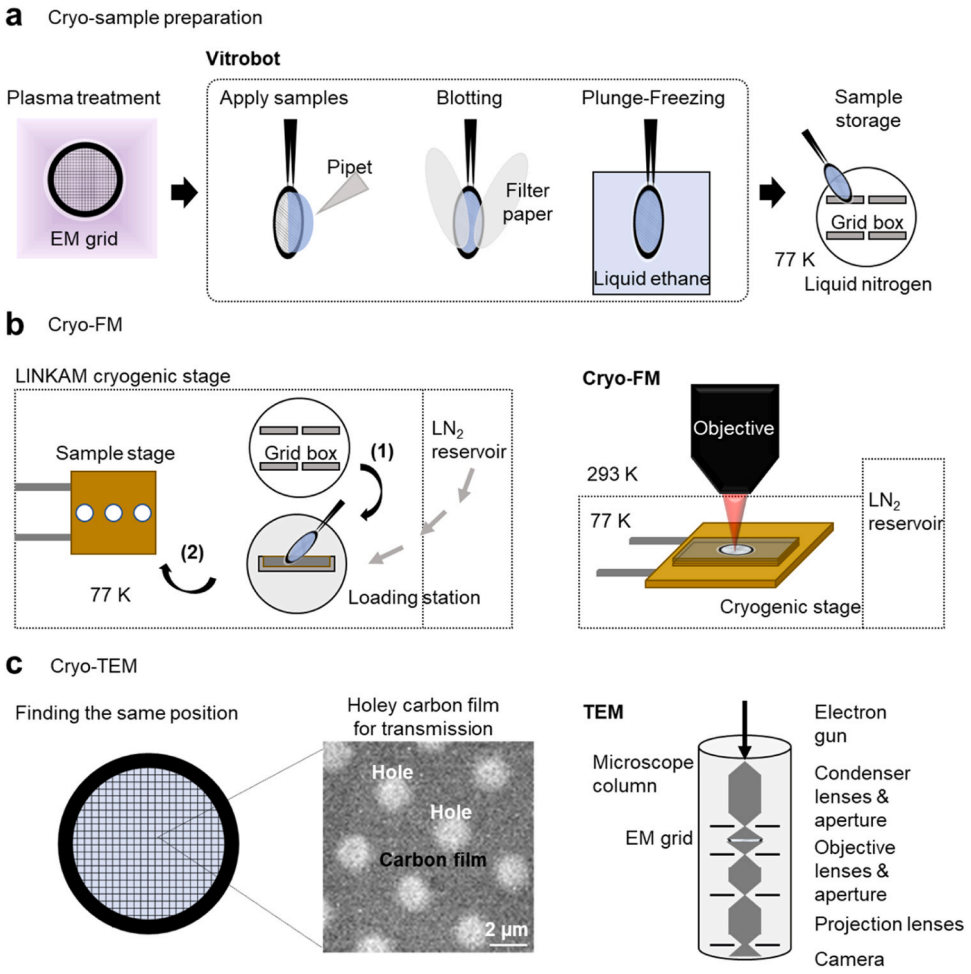

Fig. 1. General workflow of cryogenic correlative light and electron microscopy (cryo-CLEM). (a) Fluorescence-labelled samples were first diluted and vitrified using plunge vitrification. Prior to vitrification, the TEM grid is first plasma treated to make the carbon surface hydrophilic. Then the diluted sample was applied, blotted with filter paper, and plunged into liquid ethane. These steps were conducted using a Vitrobot Mark IV (Section 2.3). The vitrified samples were stored in a grid box at 77 K in liquid nitrogen before cryo-FM measurements. (b) The cryo-sample is loaded and kept at cryogenic temperatures using a LINKAM CMS196 cryo stage during cryo-FM measurements. After fluorescence imaging at 77 K, sample positions are mapped to retrieve the same position in cryo-TEM later. (c) The cryo-sample is loaded in cryo-TEM, and high-resolution images of the targeted area are obtained. To achieve higher TEM imaging contrast, holey carbon films were used.

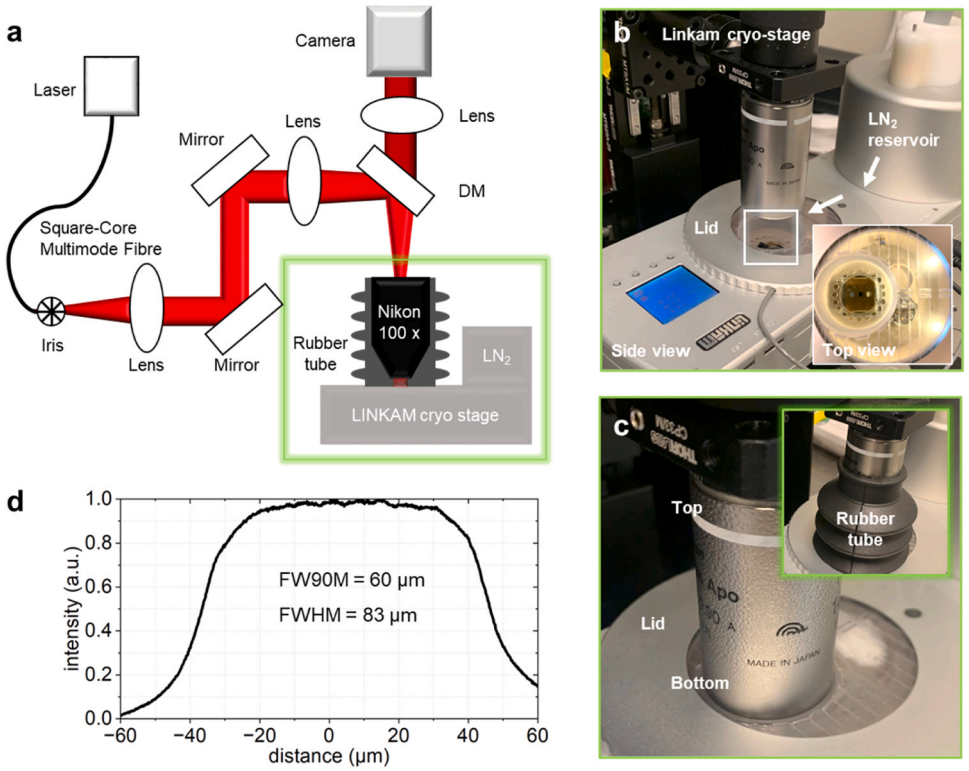

Fig. 2. Optical setup for cryogenic fluorescence microscopy (cryo-FM). (a) Schematic representation. The laser was coupled in via a square-core multimode fibre, and the iris was inserted after the fibre to adjust the beam size. Then, the beam is collimated with the lens and reflected by mirrors to the additional lens inserted for beam expansion and wide-field imaging. The beam is reflected via a dichroic mirror to the objective and illuminates the samples. The signal from samples is collected with the same objective and passes through the dichroic mirror. Then the beam is focused onto the camera using a tube lens. (b) The overview of the LINKAM cryo-stage and air type long-working distance (WD = 2.0 mm, NA 0.9) objective. The LN_2 reservoir is filled with liquid nitrogen (LN_2) supplying LN_2 to the sample stage. (c) The rubber tube was inserted to minimize the temperature difference between the sample lid (bottom) and the top side of the objective (top). Additionally, the rubber tube helps avoiding condensation of water vapor on the outside of the objective and on the sample. (d) Homogeneous laser beam intensity distribution generated by a multimode fibre with vibration motors. The beam distribution has 60 µm of full width at 90 % of the maximum intensity (FW90M), which is smaller than the size of a single grid square.

expansion and wide-field imaging. Then, the laser beam is reflected via the dichroic mirror to the objective. We chose an air-immersion objective to minimize heat transfer between the objective and the sample held at cryogenic temperatures. In our experiments, we selected an air immersion objective with a high NA of 0.9 and a long working distance of 2 mm to reach the samples through the cryo-chamber (Fig. 2b). Focusing along the Z direction is controlled by the motorized translation stage and the XY position is controlled by an internal motorized stage implemented in the LINKAM cryo-stage. The emission beam is collected with the same objective and passes through the dichroic mirror. A rubber tube was inserted between the sample and the covering part of the objective to minimize the temperature difference between the lid of the sample stage and the top side of the objective (Fig. 2c). Without the rubber tube, the objective's top side was fogged due to the temperature difference leading to weakening of the fluorescence signal over time. In addition, this inserted rubber tube helped avoiding condensation of water vapor on the outside of the objective, thus preventing ice formation or contamination on the samples. Finally, the beam is focused onto an IDS camera using a tube lens. The picture of cryogenic fluorescence microscopy setup is described in the supplementary information (Fig. S1).

For measuring the beam intensity distribution in absence of the cryo-stage, we used a fluorescent dye (Cy3). In brief, a 20 µl volume of a 1 µM dye solution was placed between two cover glasses and excited using 40 W/cm^2 laser intensity at 520 nm excitation. The uniform spatial distribution of the laser beam intensity was achieved by mode mixing the fibre with a small coin motor. Our homogeneous beam distribution has a width of 60 µm at FW90M (full width at 90 % of the maximum intensity) and 83 µm at FWHM (full width at half-maximum), thereby smaller than the size of a single grid square, ensuring that there is no further potential laser damage in other grid squares (Fig. 2d). The illumination area does not extend over the metal grid bar, ensuring that the beam effectively illuminates only a single grid square. We note that illumination over the metal grid bar potentially causes heating and concomitant devitrification of the samples.

In cryo-FM, the laser illuminates the samples on a TEM grid via the objective (Fig. 3a). The TEM grid is fixed in a grid holder connected to a metal bridge that is partially suspended in the coolant to maintain cryogenic temperatures. The TEM grid consists of many grid squares (Fig. 3b), covered with a carbon film that contains further holes where the samples are located (Fig. 3c). The width and height of a single 200 mesh TEM grid square is 90 µm, with the spacing of the metal grid being 30 µm wide. A side view of the EM grid shows the grid bar, the holey carbon film and the position of the vitreous ice layer containing the sample (Fig. 3d). The laser beam illuminates the sample, where care should be taken that heat transfer does not cause local devitrification of the sample.

Based on the laser beam intensity distribution (Fig. 2d), the expected heat transfer can be estimated. Here, we have a homogenous intensity distribution that is convenient for estimating the total impact of heat on the samples. With a typical Gaussian beam profile, the region of high laser intensity is confined to the central area, which limits the field of view (FOV) to that area where fluorophores can be effectively illuminated. In contrast, with a homogeneous beam distribution, the laser intensity is uniform across the entire FOV, allowing for a larger area to be illuminated effectively. It was previously shown that high laser power

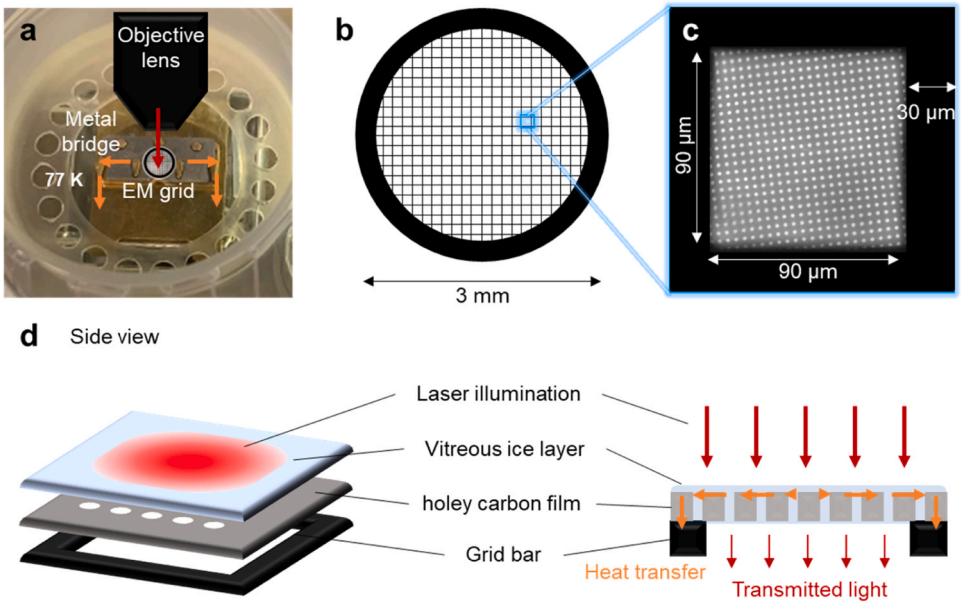

Fig. 3. Schematics of TEM grid and expected partial heat transfer from laser illumination to the sample and TEM grid. (a) Picture of the TEM grid with the grid holder on the metal bridge. Due to parts of the metal bridge being partially submerged in LN_2, the temperature of the samples during the measurements can be maintained at cryogenic temperature (77 K). (b) Schematic drawing of the TEM grid with a diameter of 3 mm featuring many grid squares. (c) Picture of a grid square. Each grid square is covered by a ~25 nm thin carbon film that has multiple holes with a 2 µm-diameter. The size of a single grid square is 90 by 90 µm, and the width of a grid bar is 30 µm for the used 200 mesh TEM grid. (d) Schematic side view of laser illumination on a single square in a TEM grid with applied samples. The laser beam (red) illuminates the vitreous sample (light blue), which is suspended by the holey carbon film (grey) on top of the grid bar (black). The expected partial heat transfer from the laser illumination (red) to the grid bar is schematically presented with orange arrows. We note that the vitreous ice layer is spanning the holes of the carbon film.

could lead to the devitrification of the cryo-samples (Chang et al., 2014; Liu et al., 2015; Tuijtel et al., 2019). Tuijtel et al. numerically calculated the expected temperature distribution (Tuijtel et al., 2019) using a finite element method (FEM) (Coady, 2012). Together with the notion that the devitrification of samples occurs at local temperatures above 136 K (Schultz, 1988), Tuijtel et al. further showed that devitrification is more dependent on laser power than the illumination time. To prevent devitrification of the ice layer and damage from the local heating induced by the laser, we experimentally determined the optimal condition for our cryo-upright microscopy setup.

The cryo-prepared acetate buffer was illuminated at 638 nm excitation wavelength for 1 min at different laser intensities calculated using the FW90M area square shape of 60 by 60 µm. The occurrence of devitrification, i.e., the presence of cubic or hexagonal ice crystals, was examined in cryo-TEM to verify the maximum allowable laser intensity. In addition, cryo-bright field microscopy with the internal LED lamp of the LINKAM cryo-stage was used to assess the damage after laser illumination.

After 1 min of illumination at 55 W/cm^2, the samples still had the vitreous ice layer intact (Fig. 4a). There was no devitrification and structural damage visible in cryo-TEM. Also, no difference was found in the cryo-bright field images after the illumination. At 330 W/cm^2 laser illumination, devitrification of the ice layer was observed in cryo-TEM, indicated by the appearance of granular structures most likely being crystals of cubic ice (Fig. 4b). Additionally, we saw the disappearance of small particles in the cryo-bright field image, likely due to the local sublimation of the ice layer after laser illumination. Especially damage on the edges of the illuminated area was clearly visible which was approximately 60 by 60 µm in size matching the measured FW90M of 60 µm (Fig. 4b). After the illumination with 1700 W/cm^2 for 1 min, severe damage to the carbon films was seen, both in cryo-TEM and cryo-bright field microscopy (Fig. 4c). Further experiments were therefore conducted under vitreous conditions (< 55 W/cm^2) to prevent damage and devitrification of samples. We note that absorption of radiation in the vitrified buffer (mostly water) on the carbon film is wavelength-dependent (Pope & Edward, 1997), so the damage from the laser can differ depending on the wavelength of illumination.

3.3. *Fluorescence imaging at cryogenic temperature*

Prior to the measurements of samples at 77 K, we first validated our microscopy setup by detecting fluorescence from fluorescently labelled beads of two different sizes (Fig. S2). Fluorescent beads were prepared on the TEM grid using plunge-freezing (Section 2.3). We confirmed that both 780 nm and 200 nm-sized FL beads were detectable in our cryo-FM image when illuminated with 40 W/cm^2 at 520 nm laser excitation wavelength.

For fluorescence microscopy measurements at cryogenic temperatures, it is required to carefully select fluorescent dyes as they can show different characteristics at temperatures lower than room temperature (Tuijtel et al., 2019). For instance, cryogenic temperatures can reduce the photo-bleaching of fluorophores due to the lack of diffusion of small reactive molecules such as oxygen and/or hamper transformational changes of fluorophores which are often considered crucial steps of photodecomposition (Kaufmann and Hagen, 2014). Moreover, under cryogenic conditions, some fluorophores showed a higher photon budget per fluorophore compared to room temperature (Hulleman et al., 2018).

We prepared a model food emulsion with a microfluidizer incorporating the oxidation-sensitive dye, BODIPY 665/676, which we used earlier for studying lipid oxidation in food emulsions (Yang et al., 2020). BODIPY 665/676 shifts its emission wavelength from red to green upon reaction with lipid peroxyl radicals. As the dye has so far only been used at room temperature, its applicability for monitoring oxidation at cryogenic conditions (77 K) is currently unknown. After performing cryo-sample preparation and placing the samples on the cryo-FM platform, the fresh and oxidized emulsions were illuminated at 638 nm with 14 W/cm^2 and 520 nm with 40 W/cm^2, respectively, to detect non-oxidized and oxidized lipid droplets at 77 K. First, we measured the non-induced samples without dilution to check the appearance of

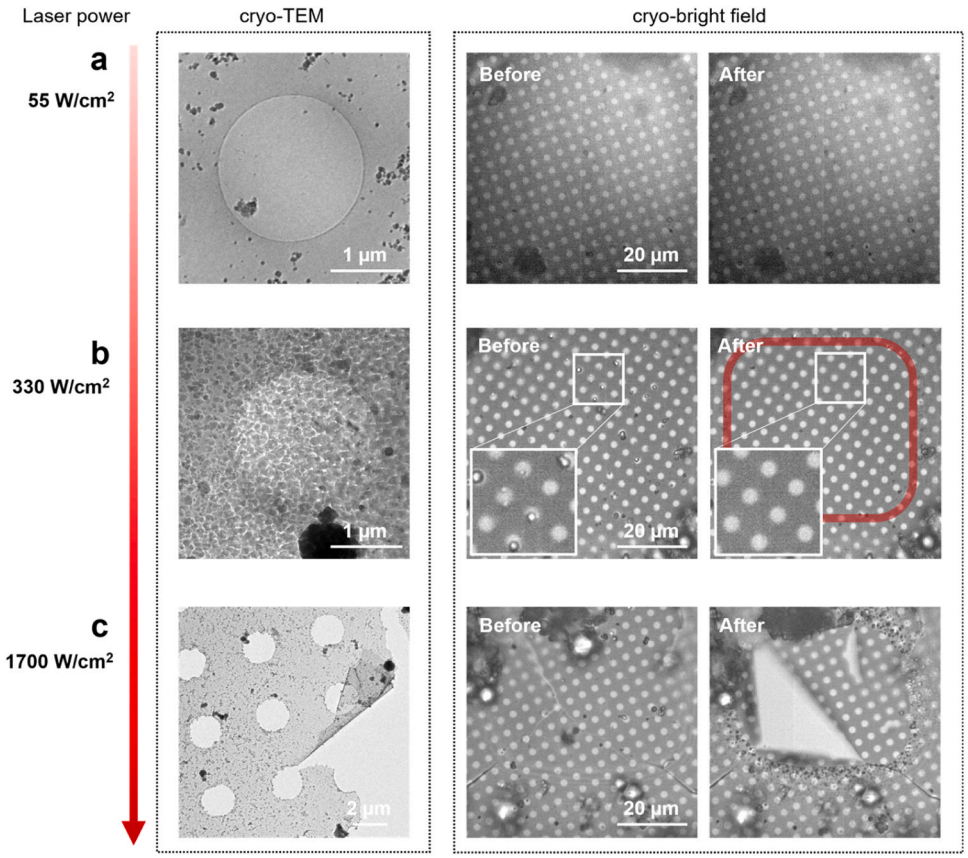

Fig. 4. Optimization of the laser illumination intensity in cryo-FM. Acetate buffer (pH 3.8) is illuminated with a laser at 638 nm for 1 min (a) Images of vitreous ice layer after the illumination with 55 W/cm^2. We found no signs of devitrification at high magnification in cryo-TEM and no visible damage to the ice layer in cryo-bright field microscopy (cryo-bright field) after laser illumination. (b) Images after the illumination with 330 W/cm^2. The devitrified ice layer is visible, indicated by the appearance of granular structures most likely being crystals of cubic ice in cryo-TEM. In the cryo-bright field images, we noticed that the particles (see white boxes) moved away after the laser illumination. The red box indicates the damaged spot from the laser, approximately the same size as the measured FW90M (60 by 60 μm). (c) Damaged samples after the illumination with 1700 W/cm^2. Damage to the carbon film was clearly visible in cryo-TEM and cryo-bright field microscopy.

fluorescence from BODIPY 665/676. In non-diluted emulsions, the packing of droplets is too dense to distinguish individual droplets (Fig. 5a & b). However, we could see a general decrease in red fluorescence (excitation at 638 nm) and an increase in green fluorescence (excitation at 520 nm) of BODIPY 665/676 in oxidized emulsions at cryogenic temperatures. To observe the effect in individual droplets, we prepared tenfold diluted samples using the acetate buffer. Under the same laser excitation conditions, we could detect the BODIPY 665/676 signals in individual droplets with non-oxidized (ex 638 nm) and oxidized (ex 520 nm) channels in the fresh (Fig. 5c) and oxidized

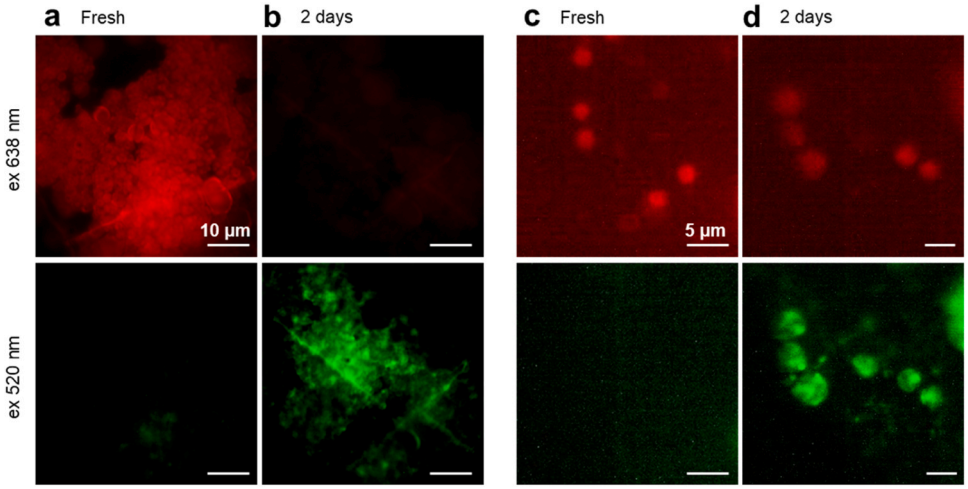

Fig. 5. Detection of BODIPY 665/676 signals at cryogenic temperature (77 K) in non-diluted (a-b) and tenfold diluted emulsions (c-d) prepared with a microfluidizer. Samples are excited at 638 nm (14 W/cm^2) and 520 nm (40 W/cm^2) to detect non-oxidized and oxidized droplets. For obtaining oxidized emulsions, the samples were incubated at 40 °C over two days in the presence of 5 mM AAPH. The contrast between (a-b) and (c-d) was adjusted for better visibility.

emulsions (Fig. 5d). The data show that the shifted emission wavelength of BODIPY 665/676 upon oxidation can be measured not only at room temperature but also at cryogenic temperature. We note that oil droplets larger than the thickness of the embedding vitrified water layer will become oblate which leads, in some cases, to elongated droplets being visible.

3.4. Interfaces of fresh and oxidized emulsions in cryo-TEM

In our previous work, we showed increased protein aggregation upon oxidation in the continuous phase separated from whole emulsions (Yang, Takeuchi, et al., 2023). Specifically, we observed oxidation of low-density lipoproteins (LDLs), which is a main ingredient of egg yolk, by confocal microscopy at μm-scale and cryo-TEM at nm-scale. Here, we want to test, (1), whether proteins at the interface also aggregate upon oxidation and, (2), whether this protein aggregation at the O/W interface is related to lipid oxidation within droplets or follows an independent mechanism.

To answer these questions, we first measured fresh and diluted model emulsions in cryo-TEM (Fig. 6). The fresh oil droplets show a smooth surface with LDLs (with a diameter of ~ 40 nm) (Anton, 2013; Anton et al., 2003) and granules from egg yolk being visible (Fig. 6a). On the other hand, phospholipids originating from LDLs and phosvitins are not observable in this sample as they are both thinly dispersed at the interface upon emulsification (Sirvente et al., 2007) and provide a contrast too low to successfully distinguish them at the interface. Upon oxidation, more aggregates and granules were observed at droplet interfaces (Fig. 6b). This finding indicates that the proteins do not only aggregate in the continuous water phase as we showed earlier (Yang, Takeuchi, et al., 2023), but also at the oil-water droplet interface as seen in Fig. 6. It should be noted that we used here stripped oil devoid of components such as tocopherols. Further, we accelerated the oxidation by adding AAPH as an oxidation initiator. Despite of using AAPH, we expect that the observed aggregation is inherent to lipid oxidation in food-grade mayonnaise. We also note that droplets larger than 1 μm are present in the emulsions, but small droplets (< 500 nm) were passively selected for TEM imaging since these are less affected by flattening during plunge vitrification.

3.5. Feasibility of cryo-correlative imaging in food oxidation studies

Cryo-fluorescence microscopy (cryo-FM) can provide functional information such as lipid and protein oxidation (Yang et al., 2020), whereas cryo-transmission electron microscopy (cryo-TEM) provides structural information of proteins and potential aggregation upon oxidation (Yang, Takeuchi, et al., 2023). Correlating the information from cryo-FM and cryo-TEM is, however, not trivial (van Driel et al., 2009). A major challenge is to find the same location in emulsions from cryo-FM and cryo-TEM. One option is to use finder grids that have each grid square marked by specific letters; thus, the same sample positions can be readily monitored in both cryo-FM and cryo-TEM. An alternative approach is to generate markers on the EM grid by devitrifying the ice on purpose using high laser intensities. This approach has the advantage that markers can be made on any type of grid.

To show the feasibility of cryo-correlative imaging in food oxidation studies, the dilute emulsions were prepared on either a Finder/Au or a Copper/Quantifoil TEM grid. We first measured the fluorescence images of emulsions using BODIPY 665/676 in cryo-FM before imaging the same droplets in cryo-TEM. With the Finder/Au TEM grid, the droplets could be easily tracked based on the letter markers (Fig. 7a). With the Copper/Quantifoil TEM grid, a damaged artifact was intentionally made with high laser power (1700 W/cm^2 at 638 nm excitation) on the grid (Fig. 7b). This approach enables tracking in cryo-TEM together with the asymmetric centre mark of the TEM grid (Fig. 7b inset). Again, this method was used to correlate the same oil droplets in cryo-FM and cryo-TEM. We confirmed that both methods are applicable for finding the same position in cryo-FM and cryo-TEM.

We could detect individual oil droplets using BODIPY 665/676 in

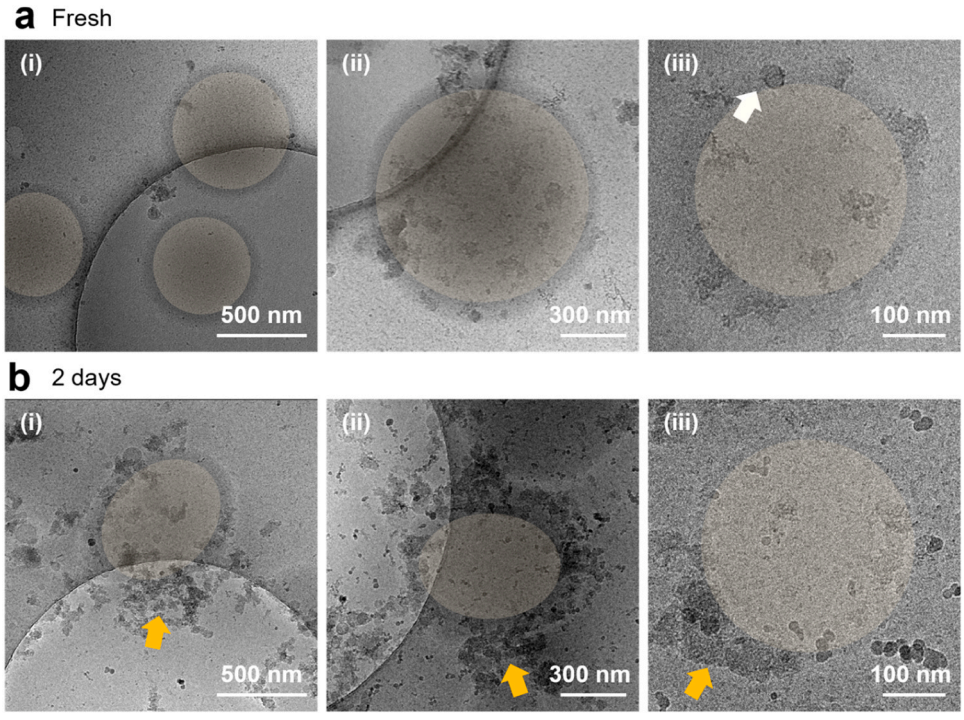

Fig. 6. Cryo-TEM images of fresh (**a**) and oxidized (**b**) model food emulsions prepared with a microfluidizer. For visual guidance, the oil droplets are highlighted in yellow. LDL particles and their aggregates are indicated by white and yellow arrows, respectively. For the oxidized samples, the emulsions were incubated at 40 °C for 2 days with 5 mM of AAPH. Cryo-TEM images in fresh and oxidized emulsions were acquired at magnifications of 6500 × (i and ii) and 24,000×(iii). A nominal defocus of − 20 μm and − 5 μm was applied for magnifications of 6500 × and 24,000×, respectively. Contrast and brightness were adjusted for better visibility.

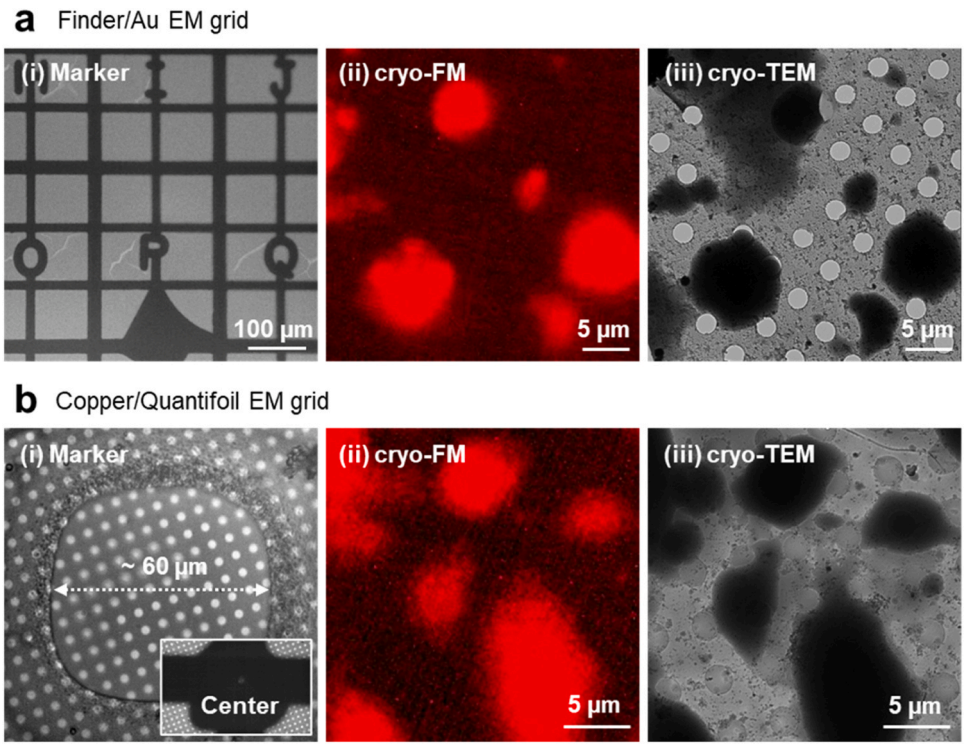

Fig. 7. Cryo-correlative light and electron microscopy (cryo-CLEM) images of fresh model emulsions prepared with a lab-scale colloid mill on Finder/Au (**a**) and prepared with a microfluidizer on Copper/Quantifoil TEM grids (b). (a) The letters on Finder/Au TEM grid (i) were used to track oil droplets with native fluorescence of BODIPY 665/676 in cryo-FM (ii) and in cryo-TEM (iii). (b) The markers on the Copper/Quantifoil TEM grid were made with the illumination at 1700 W/cm^2 of 638 nm excitation for 1 min (i). Employing either marker approach, the same droplets could be co-localised in cryo-FM (ii) and cryo-TEM (iii).

cryo-FM and observe the same droplets in cryo-TEM (Fig. 7). However, resolving droplet interfaces consisting of protein granules in large droplets (> 500 nm) was not possible in cryo-TEM as the droplets were too large for the electron beam to penetrate. With common lab-scale emulsification methods such as colloid mills, microfluidizers, and high-pressure homogenizers, polydisperse emulsions are obtained in which the diameter of droplets ranges from 200 nm to 10 µm. Unfortunately, the fluorescence signal of droplets, that would be small enough to be resolved in cryo-TEM, is too weak to be detected in the presence of large droplets. In cryo-FM, only bright 200 nm beads, but no small droplets, were detectable (Fig. S2). This limitation calls for a sample preparation procedure where, for polydisperse emulsions, small droplets are separated from larger ones. Such a procedure would rely on the assumption that emulsifier composition at the interface is not perturbed by a mild separation procedure. This assumption is typically valid in case of food emulsions in which emulsifiers are kinetically trapped at the interface (Berton-Carabin et al., 2018b). Another assumption of adopting such a procedure would be that small droplets have a similar coverage of proteins as larger ones. Alternatively, microfluidic emulsification can be used since it provides monodisperse emulsions (ten Klooster, Berton-Carabin, & Schroën, 2022). In recent pre-printed work (Yang, ten Klooster et al., 2023), we observed different protein oxidation behaviour at droplet interfaces for emulsions prepared with microfluidic emulsification and conventional emulsification using a colloid mill. This finding could be explained by different arrangements of protein emulsifier at droplet interfaces. Such experimental manipulation of emulsifier arrangement opens an experimental route to deploy our cryo-CLEM workflow to investigate relation between protein coverage of droplet interfaces and the interplay of lipid and protein oxidation.

4. Conclusions

We demonstrated the first implementation of correlative imaging of cryo-FM and cryo-TEM for use in food oxidation studies. Experimental improvements in cryo-FM have been achieved, including the prevention of fogging, and tuning the size of the laser beam, thereby achieving a homogenous laser intensity distribution over the field of view of interest. Using cryo-TEM, we could observe more protein aggregates at the interface of oxidized emulsions than in fresh emulsions. Moreover, we showed lipid oxidation in cryo-condition by monitoring the spectral shift of BODIPY 665/676, thus opening the way for future cryo-correlative oxidation studies. We demonstrated the feasibility of correlative imaging for lipid oxidation and protein structure changes at the oil-water interface upon oxidation. A current limitation of cryo-CLEM is that only small droplets (< 500 nm diameter) can be studied and that fluorescence originating from nearby larger droplets needs to be avoided. Follow-up work on polydisperse emulsions and more realistic food systems will therefore either require a procedure to obtain a fraction of small droplets or an extended workflow utilising high pressure freezing (HPF) and cryo-microtomy that we outline in the supplementary information (Fig. S3). We note that such procedures will not be required for mono-disperse small droplet distributions obtained by microfluidic emulsification. By comparing small droplets separated from polydisperse system with samples prepared using HPF and cryo-microtomy, cryo-CLEM will help to characterise the interplay between droplet coverage and lipid oxidation.

Funding statement

This work was financially supported by the Netherlands Organisation for Scientific Research (NWO) in the framework of the Innovation Fund for Chemistry and from the Ministry of Economic Affairs in the framework of the 'TKI/PPS-Toeslagregeling', with Grant No. of 731.017.301.

CRediT authorship contribution statement

Suyeon Yang: Writing – original draft, Visualization, Validation, Investigation. **Machi Takeuchi:** Writing – original draft, Visualization, Validation, Investigation. **Rick R.M. Joosten** Methodology, Investigation. **John P.M. van Duynhoven:** Writing – review & editing, Supervision, Conceptualization. **Heiner Friedrich:** Writing – review & editing, Supervision, Conceptualization. **Johannes Hohlbein:** Writing – review & editing, Supervision, Conceptualization.

Declaration of Competing Interest

J.P.M.v.D. is employed by a company that manufactures and markets mayonnaise. The other authors declare that they have no known competing financial interests or personal relationships that could influence the work reported in this paper.

Data availability

The experimental raw data is available on https://doi.org/10.5281/zenodo.10148508.

Acknowledgments

We would like to thank our colleagues in the LICENSE consortium for helpful discussions. We thank dr. Georg Wolff and dr. Montserrat Bárcena at Leiden University Medical Center for their expert help on the cryo-stage instrumentation.

Appendix A. Supporting information

Supplementary data associated with this article can be found in the online version at doi:10.1016/j.foostr.2024.100365.

References

Anton, M. (2013). Egg yolk: Structures, functionalities and processes. *Journal of the Science of Food and Agriculture, 93*(12), 2871–2880. https://doi.org/10.1002/jsfa.6247

Anton, M., Martinet, V., Dalgalarrondo, M., Beaumal, V., David-Briand, E., & Rabesona, H. (2003). Chemical and structural characterisation of low-density lipoproteins purified from hen egg yolk. *Food Chemistry, 83*(2), 175–183. https://doi.org/10.1016/S0308-8146(03)00060-8

Ayache, J., Beaunier, L., Boumendil, J., Ehret, G., & Laub, D. (2010). Physical and chemical mechanisms of preparation techniques. *Sample Preparation Handbook for Transmission Electron Microscopy*, 83–123. https://doi.org/10.1007/978-0-387-98182-6_5

Berton, C., Genot, C., & Ropers, M. H. (2011). Quantification of unadsorbed protein and surfactant emulsifiers in oil-in-water emulsions. *Journal of Colloid and Interface Science, 354*(2), 739–748. https://doi.org/10.1016/j.jcis.2010.11.055

Berton, C., Ropers, M. H., Viau, M., & Genot, C. (2011). Contribution of the interfacial layer to the protection of emulsified lipids against oxidation. *Journal of Agricultural and Food Chemistry, 59*(9), 5052–5061. https://doi.org/10.1021/jf200086n

Berton-Carabin, C. C., Ropers, M. H., & Genot, C. (2014). Lipid oxidation in oil-in-water emulsions: Involvement of the interfacial layer. *Comprehensive Reviews in Food Science and Food Safety, 13*(5), 945–977. https://doi.org/10.1111/1541-4337.12097

Berton-Carabin, C. C., Sagis, L., & Schroën, K. (2018a). Formation, structure, and functionality of interfacial layers in food emulsions. *Annual Review of Food Science and Technology, 9*, 551–587. https://doi.org/10.1146/annurev-food-030117-012405

Berton-Carabin, C. C., Sagis, L., & Schroën, K. (2018b). Formation, structure, and functionality of interfacial layers in food emulsions. *Annual Review of Food Science and Technology*. https://doi.org/10.1146/annurev-food-030117

Brown, E., & Verkade, P. (2010). The use of markers for correlative light electron microscopy. *Protoplasma, 244*(1), 91–97. https://doi.org/10.1007/s00709-010-0165-1

Chang, Y. W., Chen, S., Tocheva, E. I., Treuner-Lange, A., Löbach, S., Søgaard-Andersen, L., & Jensen, G. J. (2014). Correlated cryogenic photoactivated localization microscopy and cryo-electron tomography. *Nature Methods, 11*(7), 737–739. https://doi.org/10.1038/nmeth.2961

Coady, J. (2012). Finite Element Method in MATLAB. *Particle in Cell*. ⟨https://www.particleincell.com/2012/matlab-fem/⟩.

Dahl, R., & Staehelin, L. A. (1989). High-pressure freezing for the preservation of biological structure: Theory and practice. *Journal of Electron Microscopy Technique, 13*(3), 165–174. https://doi.org/10.1002/JEMT.1060130305

de Boer, P., Hoogenboom, J. P., & Giepmans, B. N. G. (2015). Correlated light and electron microscopy: Ultrastructure lights up! *Nature Methods, 12*(6), 503–513. https://doi.org/10.1038/nmeth.3400

Giepmans, B. N. G. (2008). Bridging fluorescence microscopy and electron microscopy. *Histochemistry and Cell Biology* (Vol. 130,(Issue 2), 211–217. https://doi.org/10.1007/s00418-008-0460-5

Hulleman, C. N., Li, W., Gregor, I., Rieger, B., & Enderlein, J. (2018). Photon yield enhancement of red fluorophores at cryogenic temperatures. *ChemPhysChem, 19*(14), 1774–1780. https://doi.org/10.1002/CPHC.201800131

Kaufmann, R., & Hagen, C. (2014). Fluorescence cryo-microscopy: Current challenges and prospects. *Current Opinion in Chemical Biology*. https://doi.org/10.1016/j.cbpa.2014.05.007

Kuo, J. (2007). In J. Kuo (Ed.), *369. Electron microscopy: Methods and protocols*. Springer Science & Business Media. https://doi.org/10.1007/978-1-59745-294-6.

Liu, B., Xue, Y., Zhao, W., Chen, Y., Fan, C., Gu, L., Zhang, Y., Zhang, X., Sun, L., Huang, X., Ding, W., Sun, F., Ji, W., & Xu, T. (2015). Three-dimensional super-resolution protein localization correlated with vitrified cellular context. *Scientific Reports, 5*. https://doi.org/10.1038/srep13017

McClements, D. J. (2015). *Food Emulsions: Principles, Practices, and Techniques* (Third Edition, pp. 1–676). https://doi.org/10.1201/b18868. 10.1201/b18868

McClements, D. J., & Decker, E. A. (2000). Lipid oxidation in oil-in-water emulsions: Impact of molecular environment on chemical reactions in heterogeneous food systems. *Journal of Food Science, 65*(8), 1270–1282. https://doi.org/10.1111/j.1365-2621.2000.tb10596.x

Mironov, A. A., & Beznoussenko, G. v (2009). Correlative microscopy: A potent tool for the study of rare or unique cellular and tissue events. *Journal of Microscopy, 235*(3), 308–321. https://doi.org/10.1111/j.1365-2818.2009.03222.x

Muller-Reichert, T., & Verkade, P. (2014). *Correlative light and electron microscopy II*. Academic Press.

Murk, J. L. A. N., Posthuma, G., Koster, A. J., Geuze, H. J., Verkleij, A. J., Kleijmeer, M. J., & Humbel, B. M. (2003). Influence of aldehyde fixation on the morphology of endosomes and lysosomes: Quantitative analysis and electron tomography. *Journal of Microscopy, 212*(1), 81–90. https://doi.org/10.1046/J.1365-2818.2003.01238.X

Pope, R. M., & Edward, S. F. (1997). Absorption spectrum (380–700 nm) of pure water. II. Integrating cavity measurements. *Applied Optics, 36*(33), 8710–8723. https://doi.org/10.1364/AO.36.008710

Schnell, U., Dijk, F., Sjollema, K. A., & Giepmans, B. N. G. (2012). Immunolabeling artifacts and the need for live-cell imaging. *Nature Methods, 9*(2), 152–158. https://doi.org/10.1038/nmeth.1855

Schultz, P. (1988). Cryo-electron microscopy of vitrified specimens. *Quarterly Reviews of Biophysics, 21*(2), 129–228. https://doi.org/10.1017/S0033583500004297

Sirvente, H., Beaumal, V., Gaillard, C., Bialek, L., Hamm, D., & Anton, M. (2007). Structuring and functionalization of dispersions containing egg yolk, plasma and granules induced by mechanical treatments. *Journal of Agricultural and Food Chemistry, 55*(23), 9537–9544. https://doi.org/10.1021/jf0719398

Steinbrecht, R., & Zierold, K. (Eds.). (2012). *Cryotechniques in biological electron microscopy*. Heidelberg: Springer Berlin. https://doi.org/10.1007/978-3-642-72815-0.

ten Klooster, S., Berton-Carabin, C., & Schroën, K. (2022). Design insights for upscaling spontaneous microfluidic emulsification devices based on behavior of the Upscaled Partitioned EDGE device. *Food Research International.* , Article 112365. https://doi.org/10.1016/j.foodres.2022.112365

Tuijtel, M. W., Koster, A. J., Jakobs, S., Faas, F. G. A., & Sharp, T. H. (2019). Correlative cryo super-resolution light and electron microscopy on mammalian cells using fluorescent proteins. *Scientific Reports, 9*(1), 1–11. https://doi.org/10.1038/s41598-018-37728-8

van Driel, L. F., Valentijn, J. A., Valentijn, K. M., Koning, R. I., & Koster, A. J. (2009). Tools for correlative cryo-fluorescence microscopy and cryo-electron tomography applied to whole mitochondria in human endothelial cells. *European Journal of Cell Biology, 88*(11), 669–684. https://doi.org/10.1016/J.EJCB.2009.07.002

van Elsland, D. M., Bos, E., Overkleeft, H. S., Koster, A. J., & van Kasteren, S. I. (2015). The potential of bioorthogonal chemistry for correlative light and electron microscopy: A call to arms. *Journal of Chemical Biology, 8*(4), 153–157. https://doi.org/10.1007/s12154-015-0134-4

van Huis, M. A., & Friedrich, H. (2014). Electron microscopy techniques. *Nanoparticles: Workhorses of Nanoscience*, 191–221. https://doi.org/10.1007/978-3-662-44823-6_7

Wang, Y., Friedrich, H., Voets, I. K., Zijlstra, P., & Albertazzi, L. (2021). Correlative imaging for polymer science. *Journal of Polymer Science, 59*(12), 1232–1240. https://doi.org/10.1002/POL.20210013

Wolff, G., Hagen, C., Grünewald, K., & Kaufmann, R. (2016). Towards correlative super-resolution fluorescence and electron cryo-microscopy. *Biology of the Cell, 108*(9), 245–258. https://doi.org/10.1111/boc.201600008

Yang, J., & Xiong, Y. L. (2015). Inhibition of lipid oxidation in oil-in-water emulsions by interface-adsorbed myofibrillar protein. *Journal of Agricultural and Food Chemistry, 63*(40), 8896–8904. https://doi.org/10.1021/acs.jafc.5b03377

Yang, S., Verhoeff, A. A., Merkx, D. W. H., van Duynhoven, J. P. M., & Hohlbein, J. (2020). Quantitative spatiotemporal mapping of lipid and protein oxidation in mayonnaise. *Antioxidants 2020, 9*(12), 1278. https://doi.org/10.3390/ANTIOX9121278

Yang, S., Takeuchi, M., Friedrich, H., van Duynhoven, J. P. M., & Hohlbein, J. (2023). Unravelling mechanisms of protein and lipid oxidation in mayonnaise at multiple

length scales. *Food Chemistry, 402*, Article 134417. https://doi.org/10.1016/J.FOODCHEM.2022.134417

Yang, S., ten Klooster, S., Nguyen, K.A., Hennebelle, M., Berton-Carabin, C., Schroën, K., Van Duynhoven, J.P.M., & Hohlbein, J. (2023). *Droplet size dependency and spatial heterogeneity of lipid oxidation in whey protein isolate-stabilized emulsions*. https://doi.org/10.26434/CHEMRXIV-2023-QXN0J.

Zhu, Z., Zhao, C., Yi, J., Liu, N., Cao, Y., Decker, E. A., & McClements, D. J. (2018). Impact of interfacial composition on lipid and protein co-oxidation in oil-in-water emulsions containing mixed emulisifers. *Journal of Agricultural and Food Chemistry, 66*(17), 4458–4468. https://doi.org/10.1021/acs.jafc.8b00590